CELLULAR NEUROSCIENCE

Parkin regulates amino acid homeostasis at mitochondria-lysosome (M/L) contact sites in Parkinson's disease

Wesley Peng, Leonie F. Schröder, Pingping Song, Yvette C. Wong, Dimitri Krainc*

Copyright © 2023 The Authors, some rights reserved; exclusive licensee American Association for the Advancement of Science. No claim to original U.S. Government Works. Distributed under a Creative Commons Attribution NonCommercial License 4.0 (CC BY-NC).

Mutations in the E3 ubiquitin ligase parkin are the most common cause of early-onset Parkinson's disease (PD). Although parkin modulates mitochondrial and endolysosomal homeostasis during cellular stress, whether parkin regulates mitochondrial and lysosomal cross-talk under physiologic conditions remains unresolved. Using transcriptomics, metabolomics and super-resolution microscopy, we identify amino acid metabolism as a disrupted pathway in iPSC-derived dopaminergic neurons from patients with parkin PD. Compared to isogenic controls, parkin mutant neurons exhibit decreased mitochondria-lysosome contacts via destabilization of active Rab7. Subcellular metabolomics in parkin mutant neurons reveals amino acid accumulation in lysosomes and their deficiency in mitochondria. Knockdown of the Rab7 GTPase-activating protein TBC1D15 restores mitochondria-lysosome tethering and ameliorates cellular and subcellular amino acid profiles in parkin mutant neurons. Our data thus uncover a function of parkin in promoting mitochondrial and lysosomal amino acid homeostasis through stabilization of mitochondria-lysosome contacts and suggest that modulation of interorganelle contacts may serve as a potential target for ameliorating amino acid dyshomeostasis in disease.

INTRODUCTION

Parkinson's disease (PD) is the second most common neurodegenerative disorder and is characterized by preferential loss of dopaminergic neurons in the substantia nigra pars compacta (*1*). A prominent cellular hallmark in PD is the coexistence of mitochondrial and lysosomal dysfunction (*2*–*4*), and mutations in several genes related to the function of these organelles have been linked to PD (*5*). Mutations in *PARK2*, which encodes the E3 ubiquitin ligase parkin, are the most common genetic cause of early-onset PD (*6*). Previous studies have described involvement of parkin in mitochondrial and endolysosomal homeostasis including mitophagy, mitochondrial biogenesis, and endolysosomal organization (*7*–*11*). However, whether parkin has additional functions related to mitochondrial and lysosomal cross-talk remains unclear.

A nondegradative pathway of mitochondrial and lysosomal interaction at mitochondria-lysosome contacts was recently identified (*12*). Mitochondria-lysosome contacts are tethered by the late endosomal/lysosomal Rab protein Rab7 and are untethered via the Rab7 guanosine triphosphatase–activating protein (GAP) TBC1D15 which is recruited to mitochondria (*13*). Mitochondria-lysosome contacts modulate various cellular processes including organelle dynamics and interorganelle transfer of ions and lipids (*14*–*17*). Although mitochondria-lysosome contact dysfunction has been shown in neurological diseases including *GBA1*-linked PD (*14*, *15*, *18*, *19*), how mitochondria-lysosome contacts are perturbed in other genetic forms of PD has yet to be elucidated.

Here, we used transcriptomics and metabolomics in human induced pluripotent stem cell (iPSC)–derived dopaminergic neurons to identify amino acid metabolism as a disrupted pathway in parkin PD. Using super-resolution live-cell microscopy, we observed that contact sites between mitochondria and lysosomes were reduced in parkin PD patient iPSC-derived dopaminergic neurons. We found that parkin regulates mitochondria-lysosome tethering via stabilization of active, lysosome-bound Rab7, while knockdown of the Rab7 GAP TBC1D15 was sufficient to reestablish proper mitochondria-lysosome contact tethering in parkin PD neurons. Mitochondrial and lysosomal metabolomics in parkin PD neurons demonstrated accumulation of lysosomal amino acids and deficiency of mitochondrial amino acids, which was partially restored by promoting mitochondria-lysosome tethering. Thus, our data highlight a function of parkin in promoting mitochondrial and lysosomal amino acid homeostasis via regulation of mitochondria-lysosome contact sites.

RESULTS

Amino acid homeostasis is altered in parkin PD iPSC-derived dopaminergic neurons

To identify pathways dysregulated in parkin-linked PD, we used an unbiased transcriptomics and whole-cell metabolomics approach in human iPSC-derived dopaminergic neurons (Fig. 1A). We differentiated iPSCs from a patient with parkin PD and a CRISPR-generated isogenic control into dopaminergic neurons (fig. S1A). Dopaminergic neurons differentiated from parkin PD and isogenic control iPSCs expressed similar levels of tyrosine hydroxylase (TH) and other dopaminergic markers (fig. S1, B to E).

Transcriptomics showed distinct clustering of parkin PD and isogenic control dopaminergic neurons (Fig. 1B and table S1). Two hundred twenty-three genes were up-regulated, and 452 genes were down-regulated in parkin PD neurons (Fig. 1C). Pathway analysis of differentially expressed genes revealed "metabolism of amino acids and derivatives" as a significantly disrupted pathway in parkin PD neurons (Fig. 1D and fig. S2, A and B). Of the top differentially regulated genes in parkin PD neurons, multiple genes were associated with amino acid pathways (Fig. 1E and fig. S2A).

Department of Neurology, Northwestern University Feinberg School of Medicine, Chicago, Illinois 60611, USA.
*Corresponding author. Email: dkrainc@nm.org

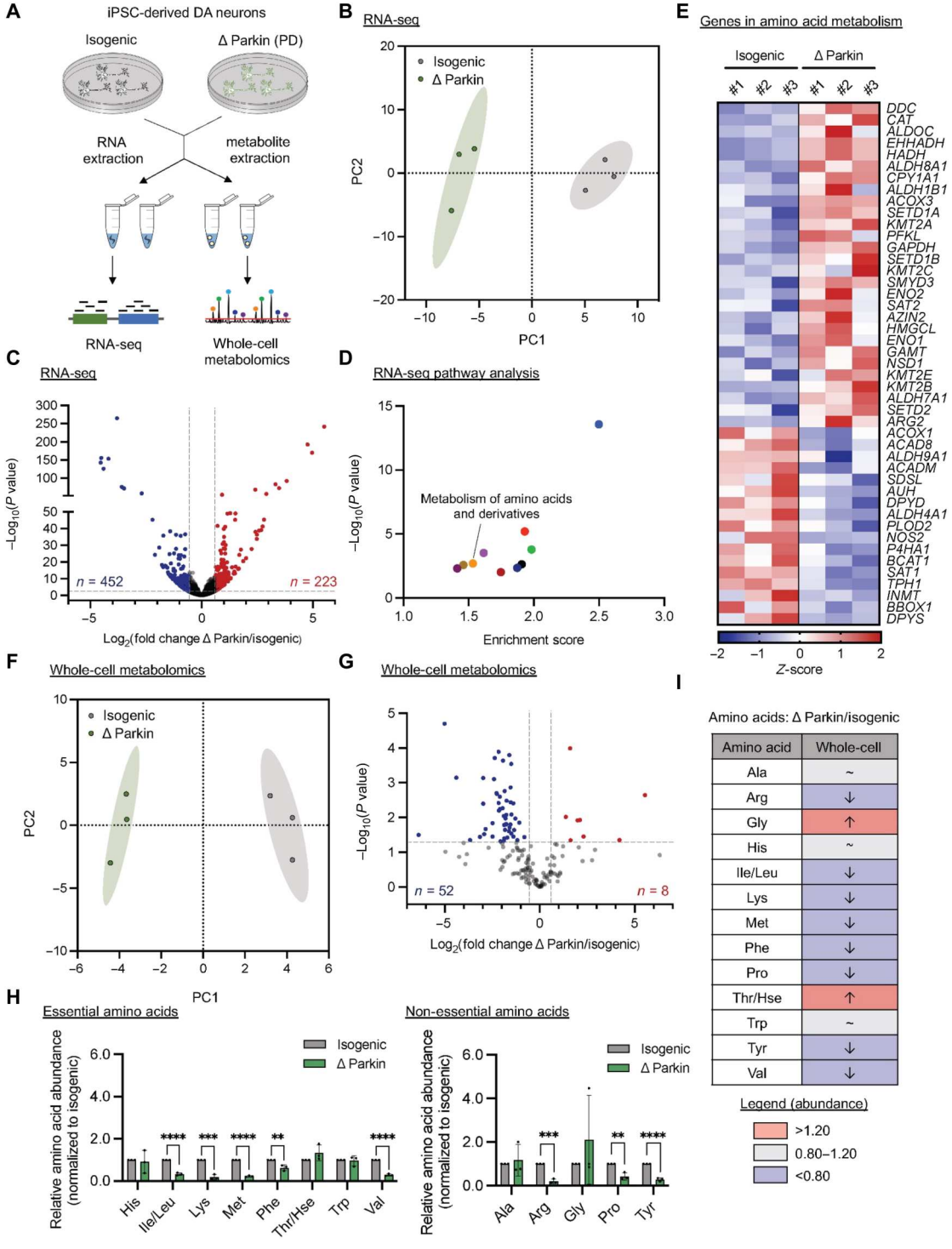

Fig. 1. Amino acid homeostasis is dysregulated in parkin PD human iPSC-derived dopaminergic neurons. (**A**) Schematic of transcriptomics and whole-cell metabolomics in Δ Parkin (PD) and isogenic control iPSC-derived dopaminergic neurons. (**B**) Principal components analysis (PCA) analysis of RNA sequencing (RNA-seq) of parkin PD and isogenic control iPSC-derived dopaminergic neurons (n = 3 biological replicates per condition). (**C** and **D**) Volcano plot (C) and pathway analysis (D) of differential genes from RNA-seq of parkin PD and isogenic control iPSC-derived dopaminergic neurons (n = 3 biological replicates per condition). (**E**) Heatmap of genes in amino acid pathways (KEGG) from RNA-seq of parkin PD and isogenic control iPSC-derived dopaminergic neurons (n = 3 biological replicates per condition). (**F**) PCA analysis of whole-cell metabolomics of parkin PD and isogenic control iPSC-derived dopaminergic neurons (n = 3 biological replicates per condition). (**G**) Volcano plot of differential metabolites from whole-cell metabolomics of parkin PD and isogenic control iPSC-derived dopaminergic neurons (n = 3 biological replicates per condition). (**H**) Relative abundance of essential and non-essential amino acids from whole-cell metabolomics of parkin PD and isogenic control iPSC-derived dopaminergic neurons (n = 3 biological replicates per condition). (**I**) Summary of whole-cell amino acid abundance in parkin PD versus isogenic controls. Data are means ± SEM [$^{**}P < 0.01$, $^{***}P < 0.001$, and $^{****}P < 0.0001$, paired two-tailed t test (H)].

We next performed whole-cell metabolomics to investigate amino acid homeostasis in parkin PD versus isogenic control dopaminergic neurons. Dopaminergic neurons from parkin PD and isogenic controls clustered distinctly (Fig. 1F), and a total of eight metabolites were up-regulated and 52 metabolites were down-regulated in parkin PD neurons (Fig. 1G and table S2). Pathway analysis of differential metabolites revealed significantly enriched amino acid pathways including "arginine biosynthesis," "phenylalanine, tyrosine, and tryptophan metabolism," and "valine, leucine, and isoleucine biosynthesis" (fig. S2, C to E). Whole-cell abundance of amino acids was altered in parkin PD neurons with significant changes in levels of the essential amino acids isoleucine/leucine, lysine, methionine, phenylalanine, and valine as well as the non-essential amino acids arginine, proline and tyrosine (Fig. 1H and fig. S2C). Whole-cell metabolomics showed a deficiency in the majority of essential and non-essential amino acids in parkin PD dopaminergic neurons (Fig. 1I).

Loss of parkin disrupts mitochondria-lysosome contact site dynamics in iPSC-derived dopaminergic neurons

Mitochondria and lysosomes are critical organelles for amino acid storage and metabolism (*20*–*22*). Because amino acid homeostasis appeared to be disrupted in parkin PD, we investigated whether parkin modulated direct contacts between mitochondria and lysosomes. Mitochondria-lysosome contacts formed dynamically in nonneuronal cells (Fig. 2A). Expression of wild-type (WT) parkin in nonneuronal cells increased the number and duration of mitochondria-lysosome contacts compared to expression of the non-ubiquitinating parkin C431S mutant, suggesting that parkin′s E3 ubiquitin ligase activity may stabilize these contact sites (Fig. 2, B to E). This effect was independent of mitochondrial and lysosomal density, which was similar between parkin WT and parkin C431S-expressing cells (fig. S3, A and B). We further evaluated parkin stabilization of mitochondria-lysosome contacts by fluorescence resonance energy transfer (FRET), which showed increased FRET efficiency between mitochondria and lysosomes in parkin WT compared to C431S-expressing cells (Fig. 2, F to H).

We next assessed whether mitochondria-lysosome contacts were disrupted in parkin PD iPSC-derived dopaminergic neurons. Mitochondria-lysosome contacts formed dynamically in iPSC-derived dopaminergic neurons (fig. S3C) as recently reported (*18*). Parkin PD neurons had decreased number and duration of mitochondria-lysosome contacts in the soma compared to isogenic controls (Fig. 3, A to C, and fig. S3, D and E). This phenotype was recapitulated in the axons of parkin PD neurons which showed reduced number and duration of mitochondria-lysosome contacts (Fig. 3, D to F, and fig. S3, F and G). Using super-resolution structured illumination microscopy (SIM) of mitochondria-lysosome contacts (Fig. 3G), we further validated decreased contact of lysosomes with mitochondria in parkin PD neurons (Fig. 3, H and I). To investigate whether reduced mitochondria-lysosome tethering in parkin PD neurons was specifically due to loss of parkin function, we evaluated mitochondria-lysosome contact dynamics in parkin PD neurons transduced with either WT parkin or the non-ubiquitinating parkin C431S mutant. WT parkin but not non-ubiquitinating parkin C431S restored mitochondria-lysosome contact formation and duration to that of isogenic control levels (fig. S3, H and I), suggesting that parkin regulation of mitochondria-lysosome contacts in human dopaminergic neurons is dependent on its ubiquitination activity. Together, these data suggest that parkin functionally promotes mitochondria-lysosome contact tethering and that loss of parkin in PD destabilizes mitochondria-lysosome contacts.

Parkin regulates mitochondria-lysosome contact sites via stabilization of active Rab7

Mitochondria-lysosome contacts are regulated by the activity of Rab7, which, in an active GTP-bound state, is found on the late endosomal/lysosomal membrane, and promotes contact tethering (*12*, *13*). Given that parkin stabilized mitochondria-lysosome contacts, we examined whether parkin modulates Rab7 activity. Using a GST-RILP pulldown assay to measure levels of active Rab7, we observed a twofold increase in active Rab7 in nonneuronal cells expressing WT parkin compared to mock- or parkin C431S-expressing cells (Fig. 4, A and B).

We previously demonstrated that parkin ubiquitinates and stabilizes Rab7 at its K38 residue (*9*). As active, lysosome-bound Rab7 promotes mitochondria-lysosome tethering, we investigated whether parkin regulates Rab7 localization. Compared to WT Rab7, the Rab7 K38R mutant, which has reduced ubiquitination by parkin (*9*), was less colocalized with lysosomes (fig. S4, A and B). Moreover, while coexpression of WT Rab7 and parkin resulted in increased Rab7 lysosomal localization, this was abrogated by expression of either mutant parkin C431S lacking its ubiquitination activity or mutant Rab7 K38R which is less ubiquitinated by parkin (Fig. 4C and fig. S4C). Thus, these results demonstrate that Rab7 lysosomal targeting is further modulated by parkin activity. To further assess the kinetics of parkin-mediated localization of Rab7 onto lysosomes, we performed fluorescence recovery after photobleaching (FRAP) of Rab7 dynamics (Fig. 4D). Expression of WT parkin promoted more rapid recovery of Rab7 onto lysosomes compared to the parkin C431S mutant, indicating that parkin dynamically promotes Rab7 lysosomal recruitment (Fig. 4, E and F, and fig. S4D).

Having demonstrated that parkin regulates Rab7 activity and lysosomal localization, we next examined whether Rab7 activity was altered in parkin PD iPSC-derived dopaminergic neurons. Compared to isogenic control neurons, parkin PD neurons showed significantly lower levels of active Rab7 (Fig. 4, G and H). Parkin PD and isogenic control neurons did not differ in either their levels of general mitochondrial and lysosomal markers (fig. S4, E and F) or expression of other mitochondria-lysosome contact–regulating proteins (Fig. 4, I and J). Because our data suggested destabilization of active Rab7 as a mechanism for reduced mitochondria-lysosome tethering in parkin PD dopaminergic neurons, we hypothesized that knockdown of TBC1D15 (Rab7 GAP) which drives contact untethering could thus help restore mitochondria-lysosome contact tethering in parkin PD neurons (fig. S4, G and H). TBC1D15 knockdown prolonged mitochondria-lysosome contacts in iPSC-derived dopaminergic neurons (fig. S4I) as has been previously described (*18*). TBC1D15 knockdown was sufficient to increase mitochondria-lysosome contact number and duration in parkin PD dopaminergic neurons to levels similar to that of isogenic control neurons, for both the soma (Fig. 5, A to D) and axons (Fig. 5, E to H). Thus, parkin modulates mitochondria-lysosome tethering via stabilization of active, lysosome-bound Rab7, and dysregulation of mitochondria-lysosome contacts in parkin PD dopaminergic

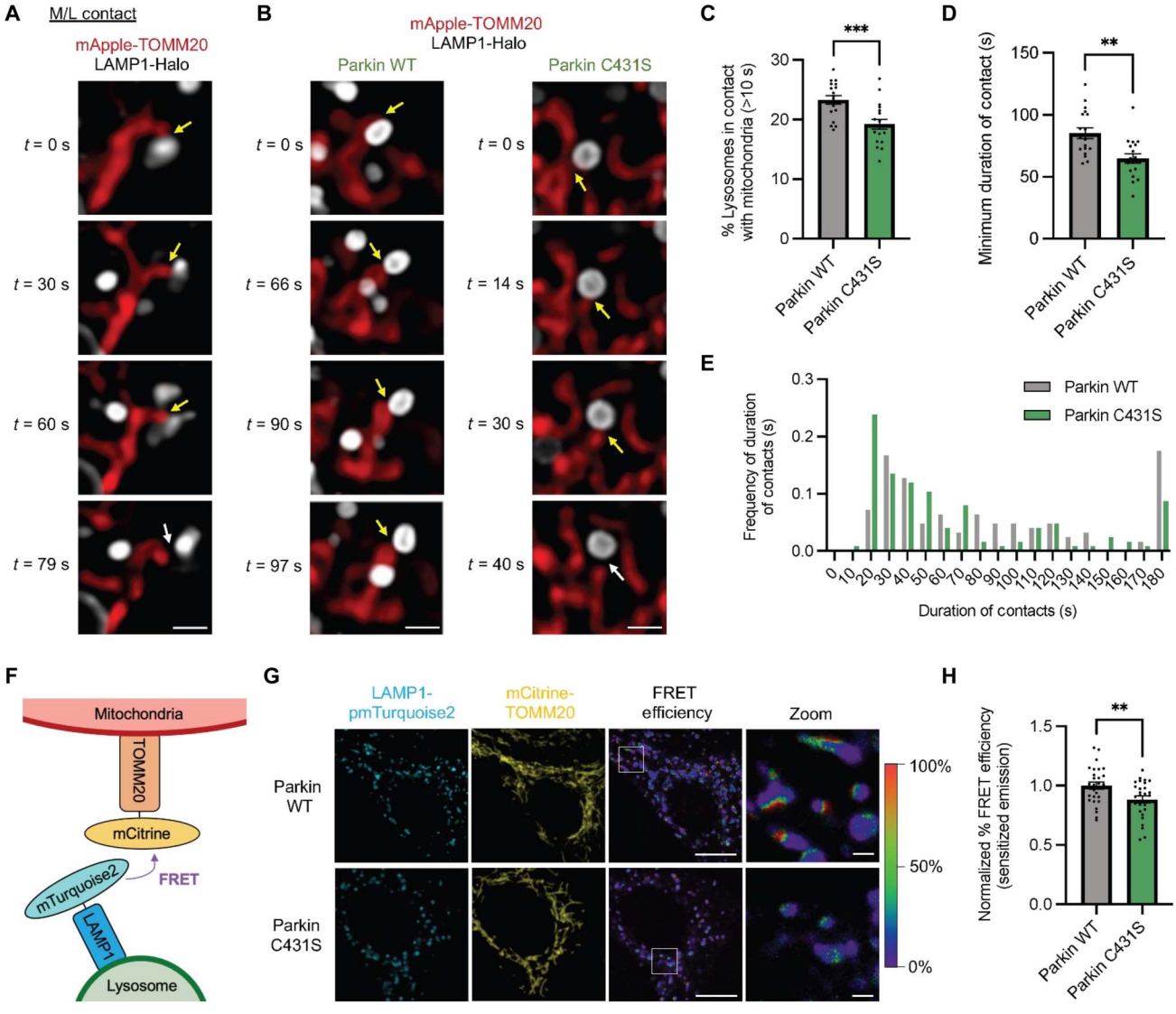

Fig. 2. Parkin stabilization of mitochondria-lysosome tethering is modulated by its ubiquitination activity. (**A**) Time-lapse images of mitochondria-lysosome (M/L) contact tethering (yellow arrow) and untethering (white arrow) in HeLa cells expressing LAMP1-Halo and mApple-TOMM20. Scale bar, 1 μm. (**B**) Time-lapse images of mitochondria-lysosome contact tethering (yellow arrow) and untethering (white arrow) in HeLa cells expressing LAMP1-Halo, mApple-TOMM20, and eGFP-Parkin or eGFP-Parkin C431S. Scale bars, 1 μm. (**C**) Quantification of percentage of lysosomes in stable contact (> 10 s) with mitochondria in HeLa cells expressing eGFP-Parkin or eGFP-Parkin C431S [from (B)] (n = 18 cells from three biological replicates per condition). (**D** and **E**) Quantification (D) and distribution (E) of minimum duration of mitochondria-lysosome contacts in HeLa cells expressing eGFP-Parkin or eGFP Parkin C431S [from (B)] (n = 126 events from 18 cells from three biological replicates per condition). (**F**) Schematic of FRET for mitochondria-lysosome contacts using FRET donor lysosomal marker LAMP1-pmTurquoise2 and FRET acceptor mitochondrial marker mCitrine-TOMM20. (**G**) Representative FRET images for mitochondria-lysosome contacts in HeLa cells expressing LAMP1-pmTurquoise, mCitrine-TOMM20, and Halo-Parkin WT or Halo-Parkin C431S. Scale bars, 10 and 1 μm (zoom). (**H**) Quantification of FRET efficiency in HeLa cells expressing LAMP1-pmTurquoise, mCitrine-TOMM20, and Halo-Parkin WT or Halo-Parkin C431S [from (G)] (n = 28 cells from three biological replicates per condition). Data are means ± SEM [**P < 0.01 and ***P < 0.001, unpaired two-tailed t test (C, D, and H)].

neurons can be mitigated by reducing levels of the Rab7 GAP TBC1D15.

Restoration of mitochondria-lysosome contact site dynamics in parkin PD dopaminergic neurons partially rescues mitochondrial and lysosomal amino acid levels

To assess whether dysregulation of mitochondria-lysosome contacts contributed to defects in amino acid homeostasis in parkin PD, we examined whether restoration of mitochondria-lysosome contact dynamics in parkin PD dopaminergic neurons could rescue whole-cell and subcellular amino acid profiles (Fig. 6A and table S3). Following TBC1D15 knockdown in parkin PD neurons, changes in whole-cell abundance of several amino acids were improved including isoleucine/leucine, valine, tyrosine, proline, lysine, and arginine (Fig. 6B). Of these, the essential amino acids isoleucine/leucine, lysine, and valine as well as the non-essential amino acids arginine, proline, and tyrosine were significantly

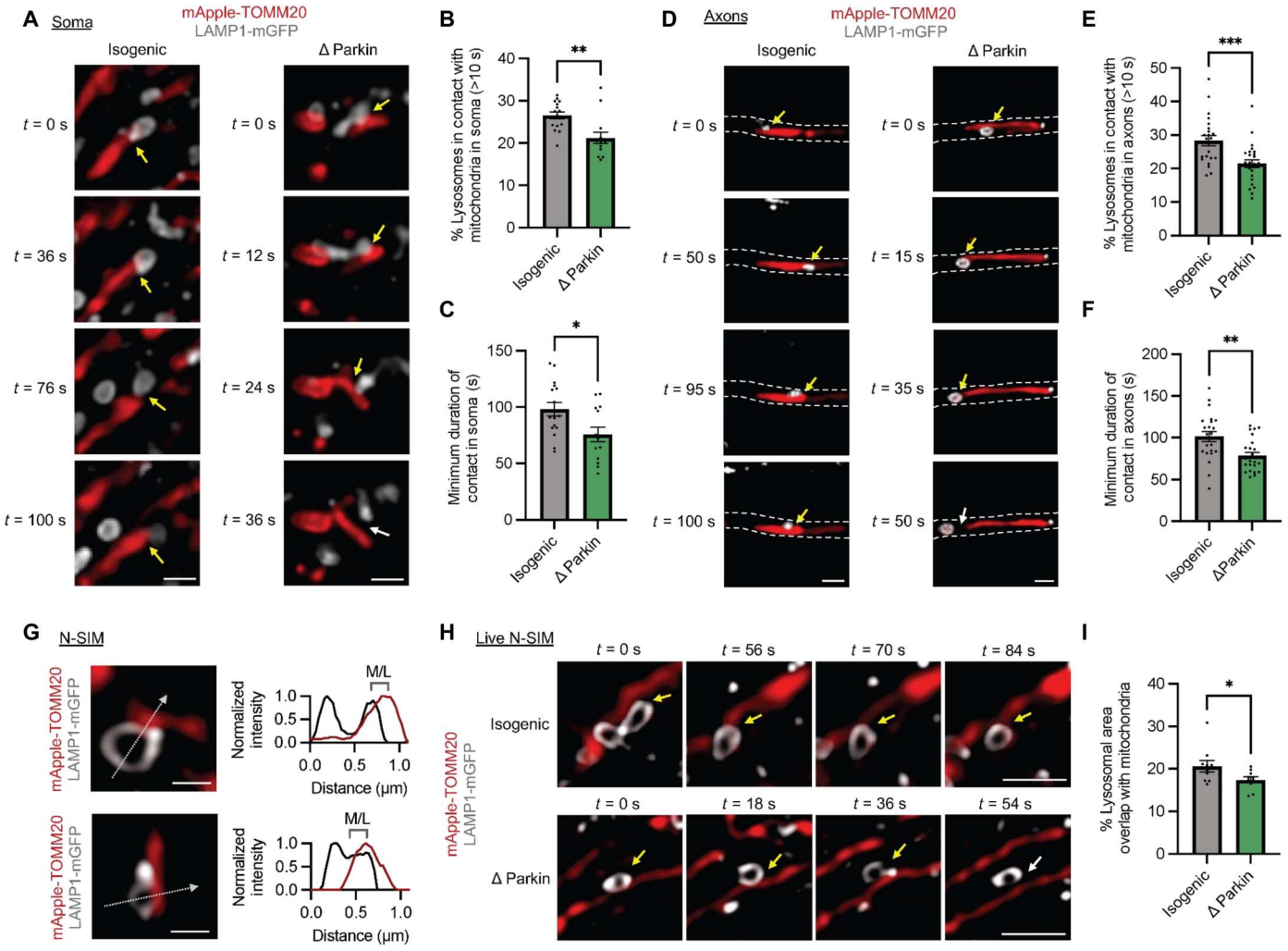

Fig. 3. Loss of parkin disrupts mitochondria-lysosome contact site dynamics in iPSC-derived dopaminergic neurons. (**A**) Time-lapse images of mitochondria-lysosome contact tethering (yellow arrow) and untethering (white arrow) in soma of Parkin PD and isogenic control iPSC-derived dopaminergic neurons expressing lentiviral LAMP1-mGFP and mApple-TOMM20. Scale bars, 1 μm. (**B** and **C**) Quantification of percentage of lysosomes in stable contact (>10 s) with mitochondria (B) and minimum duration of mitochondria-lysosome contacts (C) in soma of Parkin PD and isogenic control iPSC-derived dopaminergic neurons [from (A)] [n = 16 cells (isogenic) and 14 cells (Δ Parkin) from three biological replicates per condition]. (**D**) Time-lapse images of mitochondria-lysosome contact site tethering (yellow arrow) and untethering (white arrow) in axons of Parkin PD and isogenic control iPSC-derived dopaminergic neurons expressing LAMP1-mGFP and mApple-TOMM20. Scale bars, 1 μm. (**E** and **F**) Quantification of percentage of lysosomes in stable contact (>10 s) with mitochondria (E) and minimum duration of mitochondria-lysosome contacts (F) in axons of Parkin PD and isogenic control iPSC-derived dopaminergic neurons [from (D)] [n = 23 axons (Isogenic) and 26 axons (Δ Parkin) from three biological replicates per condition]. (**G**) N-SIM super-resolution images and line scans of mitochondria-lysosome contacts in Parkin PD and isogenic control iPSC-derived dopaminergic neurons expressing lentiviral LAMP1-mGFP and mApple-TOMM20. Scale bars, 1 μm. (**H**) N-SIM super-resolution time-lapse images of mitochondria-lysosome contact site tethering (yellow arrow) and untethering (white arrow) in Parkin PD and isogenic control iPSC-derived dopaminergic neurons expressing lentiviral LAMP1-mGFP and mApple-TOMM20. Scale bars, 1 μm. (**I**) Quantification of percentage of lysosomal area colocalized with mitochondria in Parkin PD and isogenic control iPSC-derived dopaminergic neurons [from (H)] (n = 10 cells from three biological replicates per condition). Data are means ± SEM [*P < 0.05, **P < 0.01, and ***P < 0.001, unpaired two-tailed t test (B, C, E, F, and I)].

lower in parkin PD compared to isogenic control neurons but normalized to control levels upon TBC1D15 knockdown (fig. S5A).

We next interrogated amino acid levels of mitochondria and lysosomes in parkin PD neurons to investigate how subcellular amino acid profiles respond to modulation of mitochondria-lysosome contacts. Using previously described methods (*23*, *24*), we isolated intact mitochondria and lysosomes at high purity for metabolomics analysis (fig. S5, B to E). Mitochondrial metabolomics suggested deficiencies in various amino acids in the mitochondria of parkin PD neurons (Fig. 6C). Reduced mitochondrial amino acid levels in parkin PD neurons, including the essential amino acids isoleucine/leucine, lysine, methionine, phenylalanine, threonine/homoserine, tryptophan, and valine as well as the non-essential amino acids arginine, glycine, and tyrosine, were abrogated by TBC1D15 knockdown (Fig. 6D). In contrast, lysosomal metabolomics suggested accumulation of amino acids found to be deficient in the mitochondria of PD neurons including the essential amino acids isoleucine/leucine, methionine, phenylalanine, threonine/

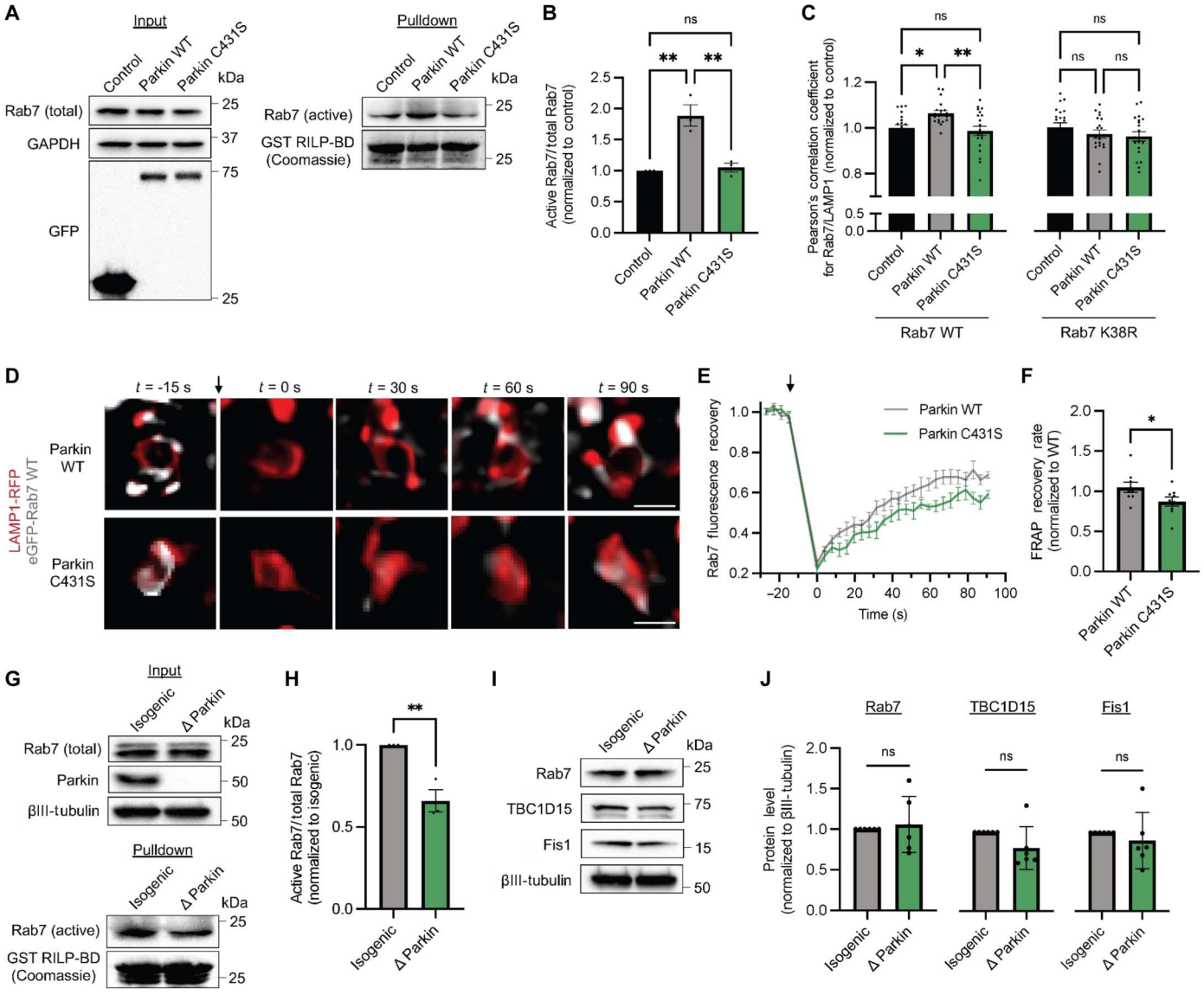

Fig. 4. Parkin regulates mitochondria-lysosome contact sites via stabilization of active, lysosome-bound Rab7. (**A**) GST-RILP pulldown to measure active Rab7-GTP in HeLa cells expressing eGFP (control), eGFP-Parkin WT, or eGFP-Parkin C431S. (**B**) Quantification of active Rab7-GTP levels in HeLa cells expressing eGFP (control), eGFP-Parkin WT, or eGFP-Parkin C431S (n = 3 biological replicates). (**C**) Pearson's correlation coefficient of eGFP-Rab7 (WT or K38R) with BFP-lysosomes in HeLa cells coexpressing mock (control), Halo-Parkin WT, or Halo-Parkin C431S (n = 20 cells from three biological replicates per condition). (**D**) Fluorescence recovery after photobleaching (FRAP) images of Rab7 onto LAMP1-positive vesicles from HeLa cells expressing LAMP1-RFP, eGFP-Rab7, and Halo-Parkin WT or Halo-Parkin C431S. Scale bars, 1 μm. (**E** and **F**) Fluorescence recovery over time (E) and quantification of FRAP recovery rate (F) of Rab7 onto LAMP1-positive vesicles in HeLa cells expressing Halo-Parkin WT or Halo-Parkin C431S [from (D)] (n = 9 cells from three biological replicates per condition). (**G**) GST-RILP pulldown to measure active Rab7-GTP in Parkin PD and isogenic control iPSC-derived dopaminergic neurons. (**H**) Quantification of active Rab7-GTP levels in Parkin PD and isogenic control iPSC-derived dopaminergic neurons [from (G)] (n = 3 biological replicates). (**I** and **J**) Representative Western blots (I) and protein quantification (J) of various mitochondria-lysosome contact site-regulating proteins in Parkin PD and isogenic control iPSC-derived dopaminergic neurons (n = 3 biological replicates). Data are means ± SEM [*P < 0.05 and **P < 0.01, ns, not significant; unpaired two-tailed t test (F, H, and J), one-way analysis of variance (ANOVA) with Tukey's post hoc test (B and C)].

homoserine, tryptophan, and valine as well as the non-essential amino acids arginine and tyrosine (Fig. 6E). The defective amino acid profiles in lysosomes from parkin PD neurons could also be partially rescued by prolongation of mitochondria-lysosome contacts via TBC1D15 knockdown (Fig. 6E).

Because prolongation of mitochondria-lysosome contacts mitigated lysosomal amino acid accumulation and mitochondrial amino acid deficiency in parkin PD neurons, we hypothesized that lysosomes may serve as a reservoir for amino acids to be supplied to mitochondria. Comparing the ratio of lysosomal to mitochondrial amino acids, we observed that parkin PD neurons exhibited a shift toward higher lysosomal amino acids (Fig. 6F). In contrast, TBC1D15 knockdown in parkin PD neurons substantially redistributed isoleucine/leucine, phenylalanine, threonine/homoserine, tryptophan, valine, arginine, and tyrosine from lysosomes to mitochondria (Fig. 6F). The ratio of lysosomal to

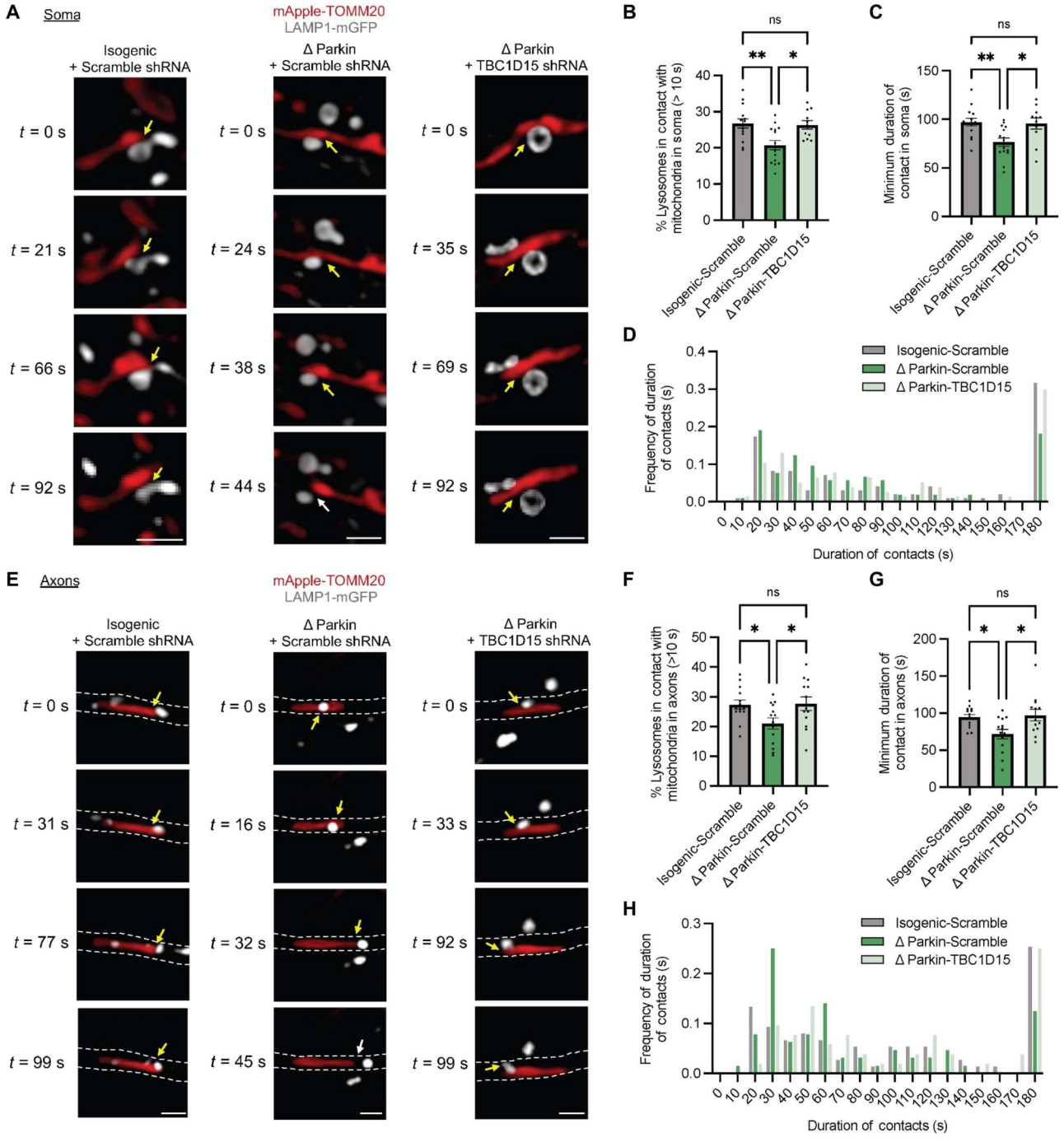

Fig. 5. Knockdown of Rab7 GAP TBC1D15 restores mitochondria-lysosome contact dynamics in parkin PD iPSC-derived dopaminergic neurons. (**A**) Time-lapse images of mitochondria-lysosome contacts in soma of Parkin PD and isogenic dopaminergic neurons expressing LAMP1-mGFP, mApple-TOMM20, and treated with TBC1D15 or Scramble shRNA. Scale bars, 1 μm. (**B**) Quantification of percentage of lysosomes in contact with mitochondria in soma of Parkin PD and isogenic neurons treated with TBC1D15 or Scramble shRNA [from (A)] [n = 14 cells (Isogenic-Scramble), 15 cells (Δ Parkin-Scramble), and 11 cells (Δ Parkin-TBC1D15) from three biological replicates per condition]. (**C** and **D**) Quantification (C) and distribution (D) of minimum duration of mitochondria-lysosome contacts in Parkin PD and isogenic neurons treated with TBC1D15 or Scramble shRNA [from (A)] [n = 98 events from 14 cells (Isogenic-Scramble), 105 events from 15 cells (Δ Parkin-Scramble), and 77 events from 11 cells (Δ Parkin-TBC1D15) from three biological replicates per condition]. (**E**) Time-lapse images of mitochondria-lysosome contacts in axons of Parkin PD and isogenic dopaminergic neurons expressing LAMP1-mGFP, mApple-TOMM20, and treated with TBC1D15 or Scramble shRNA. Scale bars, 1 μm. (**F**) Quantification of percentage of lysosomes in contact with mitochondria in axons of Parkin PD and isogenic neurons treated with TBC1D15 or Scramble shRNA [from (E)] [n = 14 axons (Isogenic-Scramble and Δ Parkin-Scramble) and 13 axons (Δ Parkin-TBC1D15) from three biological replicates per condition]. (**G** and **H**) Quantification (G) and distribution (H) of minimum duration of mitochondria-lysosome contacts in Parkin PD and isogenic neurons treated with TBC1D15 or Scramble shRNA [from (E)] [n = 75 events from 14 axons (Isogenic-Scramble), 64 events from 14 axons (Δ Parkin-Scramble), and 52 events from 13 axons (Δ Parkin-TBC1D15) from three biological replicates per condition]. Data are means ± SEM (*P < 0.05 and **P < 0.01, one-way ANOVA with Tukey's post hoc test (B, C, F, and G)].

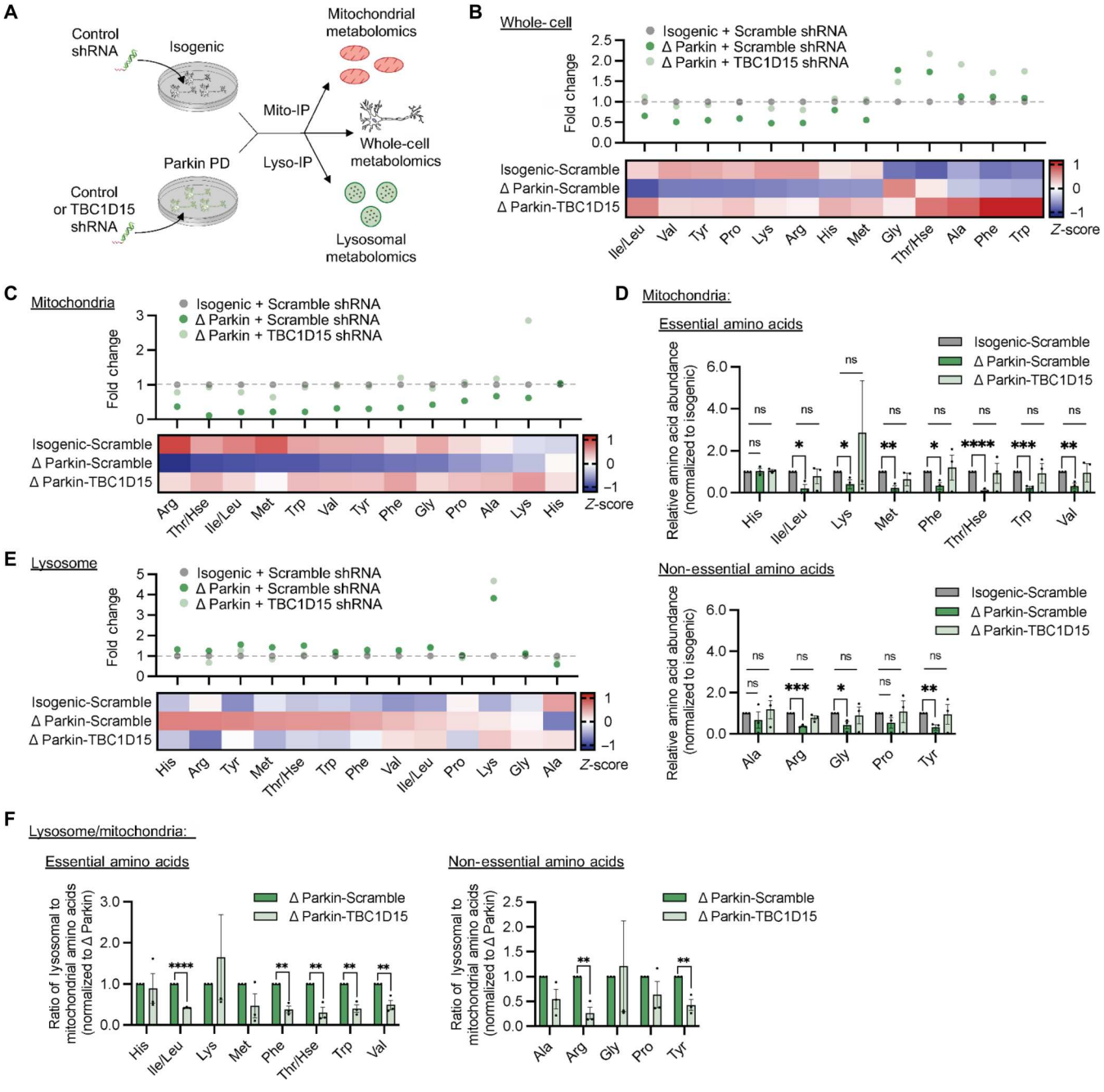

Fig. 6. Restoration of mitochondria-lysosome contact site dynamics in Parkin PD dopaminergic neurons partially rescues mitochondrial and lysosomal amino acid levels. (**A**) Schematic of whole-cell, mitochondrial, and lysosomal metabolomics in Parkin PD and isogenic control iPSC-derived dopaminergic neurons (day 70) treated with either TBC1D15 or Scramble shRNA and subjected to either Mitochondrial (Mito)- or Lysosomal (Lyso)-Immunoprecipitation (IP). (**B**) Summary heatmap and dot plot of whole-cell amino acid profiles in Parkin PD and isogenic control iPSC-derived dopaminergic neurons treated with TBC1D15 or Scramble shRNA ($n = 3$ biological replicates per condition). (**C**) Summary heatmap and dot plot of mitochondrial amino acid profiles in Parkin PD and isogenic control iPSC-derived dopaminergic neurons treated with TBC1D15 or Scramble shRNA ($n = 3$ biological replicates per condition). (**D**) Relative abundance of essential and non-essential amino acids from mitochondrial metabolomics of Parkin PD and isogenic control iPSC-derived dopaminergic neurons treated with TBC1D15 or Scramble shRNA ($n = 3$ biological replicates per condition). (**E**) Summary heatmap and dot plot of lysosomal amino acid profiles in Parkin PD and isogenic control iPSC-derived dopaminergic neurons treated with TBC1D15 or Scramble shRNA ($n = 3$ biological replicates per condition). (**F**) Ratio of lysosomal to mitochondrial amino acids in Parkin PD iPSC-derived dopaminergic neurons treated with TBC1D15 or Scramble shRNA ($n = 3$ biological replicates per condition). Data are means ± SEM [*$P < 0.05$, **$P < 0.01$, ***$P < 0.001$, and ****$P < 0.0001$, paired two-tailed t test (F) and one-way ANOVA with Dunnett's post hoc test (D)].

mitochondrial amino acids in parkin PD neurons upon TBC1D15 knockdown was similarly normalized to that of isogenic control neurons, suggesting restoration of amino acid flux between the two compartments upon stabilization of mitochondria-lysosome contacts (fig. S5F).

DISCUSSION

Together, our data identifiy a function of parkin in regulating mitochondria-lysosome contacts through the maintenance of active, lysosome-bound Rab7 and further implicates mitochondria-lysosome contacts as critical modulators of cellular and subcellular amino acid dynamics (Fig. 7, A to C). iPSC-derived dopaminergic neurons from patients with parkin PD exhibit reduced mitochondria-lysosome contacts and defective amino acid homeostasis characterized by accumulation of lysosomal amino acids and deficiency in mitochondrial amino acids. Notably, stabilization of mitochondria-lysosome contacts in parkin PD neurons partially restores whole-cell, mitochondrial, and lysosomal amino acid levels, thus highlighting a role of mitochondria-lysosome contacts in the regulation of compartment-specific amino acid profiles (fig. S6, A and B).

Our work supports the importance of parkin in regulating interactions between mitochondria and the endolysosomal system. One of the most extensively studied functions of parkin is its involvement in removing damaged mitochondria via mitophagy, and defective mitophagy has been shown in several models of parkin deficiency under conditions of mitochondrial stress (*7*, *10*). However, we found that parkin also modulates mitochondrial and lysosomal cross-talk under basal conditions by promoting nondegradative contacts between mitochondria and lysosomes to facilitate interorganelle exchange of amino acids. Thus, defects in parkin likely contribute to the pathophysiology of PD through dysregulation of multiple pathways including mitochondria-lysosome contact site dysfunction under physiologic conditions and impaired mitophagy under stress.

Disrupted mitochondria-lysosome contact dynamics and function have been described in various models of neurological disease (*14*, *15*, *18*, *19*, *25*, *26*). Here, we demonstrate that mitochondria-lysosome contacts are reduced in parkin-linked PD and that destabilization of these contact sites contributes to impaired mitochondrial and lysosomal amino acid homeostasis. Restoration of mitochondria-lysosome contacts normalizes mitochondrial and lysosomal amino acid profiles, suggesting that mitochondria-lysosome contacts may function as platforms for interorganelle amino acid transfer. Direct modulation of interorganelle contacts thus may serve as a potential therapeutic strategy for restoring metabolic defects in disease. Future studies dissecting mechanisms of amino acid signaling and transfer mediated by mitochondria-lysosome contacts will continue to inform our understanding of how mitochondria-lysosome contact site dysfunction contributes to the pathophysiology of diverse disease states.

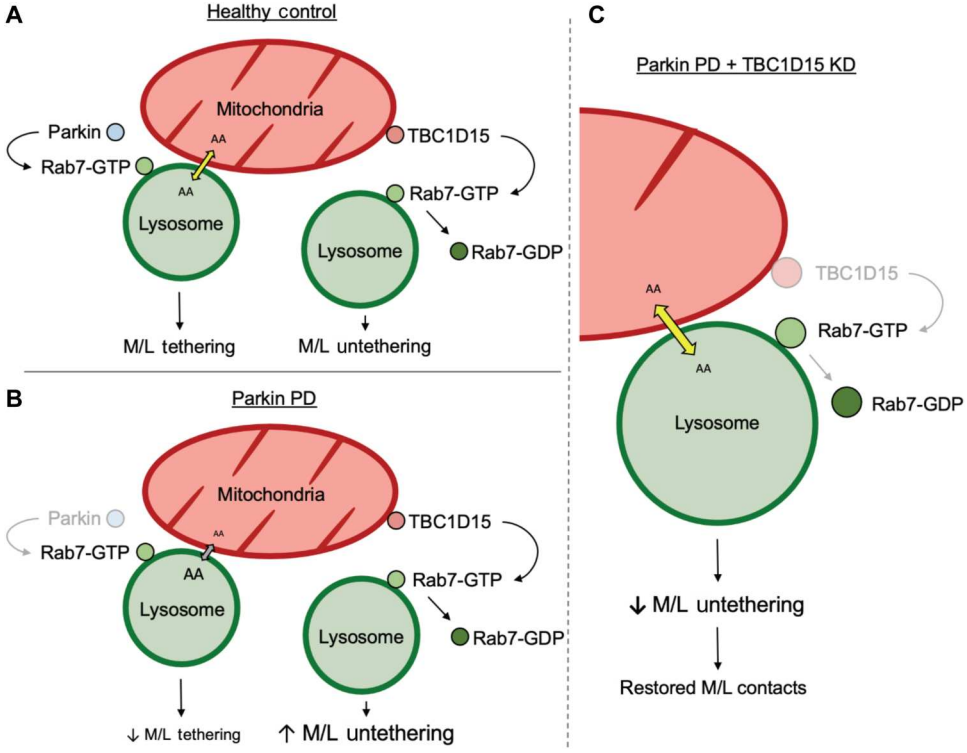

Fig. 7. Parkin promotes mitochondria-lysosome tethering and subcellular amino acid homeostasis. (**A**) Schematic of parkin regulation of mitochondria-lysosome contact sites via stabilization of active Rab7, thereby promoting mitochondrial and lysosomal amino acid homeostasis under physiologic conditions. (**B**) Schematic of loss of parkin in PD decreasing mitochondria-lysosome contact tethering due to reduced stabilization of active Rab7, thereby leading to disrupted mitochondrial and lysosomal amino acid dynamics. (**C**) Schematic of knockdown of Rab7 GAP TBC1D15 in parkin-linked PD to ameliorate mitochondria-lysosome contact site dynamics and subcellular amino acid flux.

MATERIALS AND METHODS

Experimental design

HeLa cells [American Type Culture Collection (ATCC)] were cultured in Dulbecco's modified Eagle's medium (Gibco; 11995-065) supplemented with 10% (v/v) heat-inactivated fetal bovine serum, penicillin (100 U/ml), and streptomycin (100 μg/ml). Human iPSCs derived from a PD patient harboring a parkin loss-of-function mutation (B125: homozygous c.1072del, male, age of onset: 43) as well as a CRISPR-generated isogenic control were maintained on Cultrex-coated (R&D Systems; 3434-010-02) six-well plates, cultured in mTeSR Plus Basal Medium (STEMCELL Technologies; 100-0274) with mTeSR Plus 5X Supplement (STEMCELL Technologies; 100-0275) and were passaged every 5 to 6 days. All cells were maintained at 37°C in a 5% CO_2 incubator and were previously verified by cytochrome c oxidase subunit I and short tandem repeat testing and tested for mycoplasma contamination. HeLa cells were transfected using X-tremeGENE HP (Roche; 6366546001). iPSC-derived dopaminergic neurons were transduced with the lentiviral constructs described below. For live-cell imaging, cells were grown on four-chamber glass bottom dishes (Cellvis; D35C4-20-1.5-N).

Plasmids

The following plasmids were obtained from Addgene: mApple-TOMM20-N-10 (Addgene; 54955), mCitrine-N1 (Addgene; 54594) (*27*), and EBFP2-Lysosomes-20 (Addgene; 55246) were gifts from M. Davidson; LAMP1-mGFP (Addgene; 34831) (*28*) was a gift from E. Dell-Angelica; pmTurquoise2-N1 (Addgene; 60561) (*29*) was a gift from D. Gadella; Halo-KDEL (Addgene; 124316) (*30*) was a gift from J. Wang; pEGFP-parkin WT (Addgene; 45875) (*31*) and pEGFP-parkin C431S (Addgene; 45877) (*31*) were gifts from E. Fon; EGFP-Rab7A (Addgene; 28047) (*32*) was a gift from Q. Zhong; pMXs-3xHA-EGFP-OMP25 (Addgene; 83356) (*24*) and pLJC5-LAMP1-RFP-3xHA (Addgene; 102932) (*23*) were gifts from D. Sabatini; psPAX2 (Addgene; 12260) was a gift from D. Trono; Lamp1-RFP (Addgene; 1817) (*33*) was a gift from W. Mothes; pGEX-4T-3-mR7BD (Addgene; 79149) (*34*) was a gift from A. Edinger; and Halo-TOMM20-N-10 (Addgene; 123284) was a gift from K. McGowan. Additional plasmids included the following: EGFP-Rab7 K38R (a gift from P. Song) (*9*), pLP3 (Invitrogen; K497500), and pGEX-4T-1 (Millipore Sigma; GE28-9545-49). The following plasmids were generated for this study using standard cloning procedures: LAMP1-Halo, LAMP1-pmTurquoise2, mCitrine-TOMM20, Halo-Parkin WT, Halo-Parkin C431S, pER4-mApple-TOMM20, pER4-LAMP1-mGFP, and pER4-3xHA-EGFP-OMP25.

iPSC culture and midbrain dopaminergic neuronal differentiation

Human iPSCs derived from a PD patient with a loss-of-function parkin mutation (B125: homozygous c.1072Tdel, male, age of onset: 43) and a CRISPR-generated isogenic control were cultured and maintained as described above. Directed differentiation toward dopaminergic neurons was conducted according to published small-molecule– and factor-based differentiation protocols with minor modifications (*2*, *35*, *36*). To help control neuralization variability, cells were passaged en block (size, 1 to 2 mm) between day 11 and day 14, followed by plating onto poly-D-lysine (Sigma-Aldrich; P1149)/laminin (Sigma-Aldrich; 11243217001)–coated culture dishes. Neuralization growth factors were withdrawn on day 40, and neurons were maintained in Neurobasal (Gibco; 21103) containing NeuroCult SM1 (STEMCELL Technologies; 5711). All experiments were completed between day 70 and day 80, except for those indicated.

Generation and transduction of lentiviral constructs

mApple-TOMM20-N-10 (Addgene; 54955), LAMP1-mGFP (Addgene; 34831), Halo-Parkin WT, Halo-Parkin C431S, and pMXs-3xHA-EGFP-OMP25 (Addgene; 83356) were subcloned into the pER4 lentiviral expression vector using the Nhe I/Not I cut sites. Lentiviral TBC1D15 short hairpin RNA (shRNA; Horizon Discovery; #RHS4533-EG64786) and Scramble shRNA (Horizon Discovery; #RHS6848) were obtained from Horizon Discovery. Lentiviral vectors were transfected into low passage number (< passage 10) human embryonic kidney 293FT cells using X-tremeGENE HP (Roche; 6366546001) together with helper plasmids psPAX2 (Addgene; 12260) and pLP3 (Invitrogen; K497500). Supernatants were collected after 48 hours of expression, and virus was concentrated overnight at 4°C with Lenti-X Concentrator (Clontech; 631232). Quantification of retroviral antigens was determined using a HIV-1 p24 Antigen ELISA Kit (Thermo Fisher Scientific; 22-156-700). Concentrated virus was aliquoted and stored at −80°C for future use. Lentiviral transduction of neurons of all constructs was carried out with an multiplicity of infection (MOI) of 5 for 7 days. Expression of constructs transduced by lentiviral infection was verified by either immunoblot analysis as described above or imaging as described below.

Immunocytochemistry

Immunofluorescence in iPSC-derived dopaminergic neurons was performed as previously described (*9*, *36*). Briefly, human iPSC-derived dopaminergic neurons were incubated with 0.1% saponin (Millipore Sigma; 558255) after fixation with 3% formaldehyde for 20 min (Thermo Fisher Scientific; NC9603389). Samples were then washed three times with phosphate-buffered saline (PBS) (Invitrogen; 10010-049) and incubated with primary antibodies followed by Alexa Fluor 488–conjuated goat anti-rabbit secondary antibodies (Invitrogen; A-11034), Alexa Fluor 568–conjugated goat anti-mouse secondary antibodies (Invitrogen; A-11031), or Alexa Fluor 647–conjugated goat anti-mouse antibodies (Invitrogen; A-21236). After three additional washes with PBS, the samples were mounted (Vector Labs; H-1500). Images were subsequently acquired on a Nikon W1 Spinning Disk Confocal microscope using a Plan Apo TIRF 100 × 1.49 numerical aperture (NA) differential interference contrast (DIC) oil-immersion objective. Antibodies used for immunofluorescence include anti-TH antibody (1:1000; EMD Millipore; 657012), anti-FOXA2 (1:100; Santa Cruz Biotechnology; sc-101060), and anti-LMX1A (1:1000; EMD Millipore; AB10533).

Western blot analysis

Western blot analysis was performed as previously described (*9*, *36*). Briefly, cells were scraped in cold PBS and centrifuged at 300*g* for 5 min. Pellets were resuspended in radioimmunoprecipitation assay lysis buffer (Boston BioProducts; BP-115) with protease inhibitors (Millipore Sigma; 11836170001) and incubated on ice for 30 min. Protein concentration was measured using the Bicinchoninic Acid Assay (Thermo Fisher Scientific; 23225). Samples were analyzed by

tris-glycine SDS–polyacrylamide gel electrophoresis, transferred onto nitrocellulose membranes (Bio-Rad; 170-4271), and blocked for 1 hour in 5% nonfat dry milk in Tris-buffered saline with 0.1% Tween 20 detergent (TBST). Samples were then incubated for 1 hour at room temperature or overnight with the following primary antibodies: anti-parkin (Abcam; ab15954), anti-TH (EMD Millipore; 657012), βIII-tubulin (BioLegend; 4466S), anti–glyceraldehyde phosphate dehydrogenase (Millipore; MAB374), anti–green fluorescent protein (GFP) (Santa Cruz Biotechnology; sc-9996), anti-Rab7 (Sigma-Aldrich; R8779), anti-TBC1D15 (Novus Biologicals; NBP2-20576), anti-Fis1 (Proteintech; 10956-1-AP), anti-Lamp2 (Santa Cruz Biotechnology; sc-18822), anti-Tomm20 (BD Biosciences; 612278), anti-citrate synthase (CS) (Cell Signaling Technology; 14309S), anti-membrin (Synaptic Systems; 170003), anti-calnexin (Cell Signaling Technology; 2433S), anti-PEX5 (Cell Signaling Technology; 83020S), anti-VDAC2 (Proteintech; 11663-1-AP), anti-glucocerebrosidase (Sigma-Aldrich; 4171), and anti–hemagglutinin (HA) (Cell Signaling Technologies; 3724S). Samples were then incubated with horseradish peroxidase–linked secondary antibodies for 1 hour (Jackson ImmunoResearch; 111-035-144 and 115-035-146) before imaging on the ChemiDoc XRS+.

RNA sequencing and transcriptomics analysis

Day 70 iPSC-derived dopaminergic neurons (~1×10^6 neurons) were harvested in PBS and centrifuged at 300*g* for 5 min. Pellets were homogenized using the QIAshredder spin column (Qiagen; 79654), and RNA was extracted per protocol using the RNeasy mini kit (Qiagen; 74104). mRNA libraires were constructed with the Illumina TruSeq Stranded mRNA Library Preparation Kit (Illumina; 20020594) and sequenced on an Illumina NextSeq 500 at the Northwestern University NUSeq Core Facility. DNA read quality control and RNA sequencing (RNA-seq) analysis were performed as previously described with the following modifications. The quality of the DNA reads, in FASTQ format, was evaluated using FastQC. Adapters were trimmed, and reads of poor quality or aligning to rRNA sequences were filtered. The cleaned reads were aligned to the human genome assembly using TopHat (*37*). Gene counts were quantified from BAM files using HTSeq (*38*). Normalization and differential gene expression were determined using EdgeR (*39*). The cutoff for determining significantly differentially expressed genes was with a minimum 1.5-fold change in gene expression compared to isogenic control neurons and a P value of less than 0.01. Principal components analysis (PCA) was completed using the code provided in R from MetaboAnalyst 5.0. Overrepresentation analysis of differential genes with a P value of less than 0.01 was conducted using WebGestalt (*40*). Specific amino acid pathways affected based on differentially expressed genes were identified using KEGG Mapper (*41*).

Mitochondrial and lysosomal immunoprecipitation

Mitochondrial and lysosomal immunoprecipitation were carried out as previously described (*23*, *24*). Briefly, day 70 iPSC-derived dopaminergic neurons (~7×10^6) expressing either lentiviral 3x-eGFP-OMP25 (for mitochondrial immunoprecipitation) or LAMP1-RFP-3xHA (for lysosomal immunoprecipitation) were washed on ice with liquid chromatography–mass spectrometry (LC-MS) PBS. Neurons were scraped in 1 ml of KPBS (pH 7.25) (136 mM KCl and 10 mM KH_2PO_4) and centrifuged at 1000*g* for 2 min at 4°C. Cells were resuspended in 1 ml of KPBS and immediately homogenized through a 23G syringe (Becton Dickinson; 305271), being careful to introduce as few bubbles as possible. Homogenized samples were centrifuged at 1000*g* for 3 min at 4°C, and the supernatant was applied to 200-μl anti-HA magnetic beads (Thermo Fisher Scientific; 88836). Samples were incubated on a tube rotator at 4°C for 3.5 min. The magnetic beads were washed three times with 1 ml of KPBS. Samples for immunoblot were eluted from the anti-HA magnetic beads with 40 μl of 1× Laemmli sample buffer without bromophenol blue or β-mercaptoethanol [32.9 mM tris-HCl (pH 6.8), 1.05% (w/v) SDS, and 13.15% (w/v) glycerol] and boiled for 10 min at 95°C. Immunoblot samples were then processed as described above. Samples used for metabolite extraction were processed as described below.

Metabolite extraction

For whole-cell metabolite extraction, day 70 iPSC-derived dopaminergic neurons (~1×10^6) were washed twice with 1 ml of 0.9% normal saline on ice. Neurons were then scraped in 1 ml of 80% (v/v) LC-MS–grade methanol (Thermo Fisher Scientific; A456-500). Samples were immediately freeze-thawed in liquid nitrogen three times with 30 s of vigorous vortexing between each freeze cycle. Lysed samples were stored at −80°C overnight for protein precipitation. The following morning, lysates were centrifuged at 20,000*g* for 10 min at 4°C, and the supernatant was stored at −80°C until further processing.

For mitochondrial and lysosomal metabolite extraction, organelles captured on anti-HA magnetic beads were washed with 500 μl of 80% (w/v) LC-MS–grade methanol. The sample was pipetted vigorously 10 times until homogeneous and placed on ice. Samples were vortexed 10 to 15 s every 2 min for a total of 10 min. The resulting supernatant was then stored overnight at −80°C for protein precipitation. The following morning, samples were centrifuged at 20,000*g* for 10 min at 4°C, and the resulting metabolite extract was stored at −80°C until further processing.

Metabolite measurement and metabolomics analysis

Whole-cell, mitochondrial, and lysosomal metabolite extracts were evaporated to dryness using a SpeedVac concentrator before metabolomics analysis through the Northwestern University Metabolomics Core Facility. Metabolites were reconstituted in 50% acetonitrile in analytical-grade water, vortex-mixed, and centrifuged to remove debris. Samples, normalized by total protein, were analyzed by ultrahigh-performance liquid chromatography and high-resolution mass spectrometry and tandem mass spectrometry. Specifically, the system consisted of a Thermo Q-Exactive in line with an electrospray source and an Ultimate 3000 series high-performance liquid chromatography consisting of a binary pump, degasser, and auto-sampler outfitted with an Xbridge Amide column (dimensions of 4.6 mm by 100 mm and a 3.5-μm particular size). Mobile phase A contained 95% (v/v) water, 5% (v/v acetonitrile) of 10 mM ammonium hydroxide, and 10 mM ammonium acetate (pH 9.0); and mobile phase B was 100% acetonitrile. The gradient was as follows: 0 min, 15% A; 2.5 min, 30% A; 7 min, 43% A; 16 min, 62% A; 16.1 to 18 min, 75% A; 18 to 25 min, 15% A with a flow rate of 400 μl/min. The capillary of the electrospray ionization source was set to 275°C, with sheath gas at 45 arbitrary units, auxiliary gas at 5 arbitrary units, and the spray voltage at 4.0 kV. In positive/negative polarity switching mode, an mass/charge

ratio scan range from 70 to 850 was chosen, and MS1 data were collected at a resolution of 70,000. The automatic gain control target was set at 1×10^6, and the maximum injection time was 200 ms. The top five precursor ions were subsequently fragmented, in a data-dependent manner, using the higher-energy collisional dissociation cell set to 30% normalized collision energy in MS2 at a resolution power of 17,500. Data acquisition and analysis were carried out by Xcalibur 4.1 software and Tracefinder 4.1 software, respectively. The peak area for each detected metabolite was normalized by the total ion current which was determined by integration of all of the recorded peaks within the acquisition window. Downstream analysis was carried out using Microsoft Excel. MetaboAnalyst 5.0 (https://metaboanalyst.ca) was used to identify differential metabolites, defined as a *P* value less than 0.05, for PCA and for overrepresentation analysis (*42*).

GST-RILP pulldown assay

GST-RILP pulldown assays to determine levels of active, GTP-bound Rab7 were performed as previously described with minor modifications (*34*). Briefly, GST-RILP and GST control plasmids were expressed in Lemo21(DE3) Competent *Escherichia coli* (New England BioLabs; C2528J). Bacteria were grown to an optical density of 0.6 to 0.8 before induction of recombinant protein expression with 0.5 mM isopropyl-β-D-thiogalactopyranoside for 3 hours. Bacteria were collected and lysed in the B-PER Bacterial Protein Extraction Reagent (Thermo Fisher Scientific; 78248) with 1 mM 1,4-dithiothreitol, 1 mM EDTA, and protease inhibitor (Millipore Sigma; 11836170001). Recombinant protein was purified using a pre-equilibrated 50% slurry of Glutathione Sepharose 4B beads (Millipore Sigma; GE17-0756-01) in B-PER lysis solution. Day 70 iPSC-derived dopaminergic neurons (~1.5×10^6) were pelleted at 300*g* for 5 min and lysed on ice in pulldown buffer (20 mM Hepes, 100 mM NaCl, 5 mM $MgCl_2$, and 1% Triton X-100) with protease inhibitors for 30 min. GST-control beads and GST-RILP beads were added to neuron lysates, and the samples were rocked overnight at 4°C. The following morning, samples were washed in cold, pulldown buffer twice and then centrifuged at 500*g* for 3 min at 4°C. Samples were then eluted with 50 μl of 2× Laemmli sample buffer (Sigma-Aldrich; S3401) and then subjected to Western blot analysis as described above.

Live-cell confocal microscopy

Confocal live-cell imaging was conducted on a Nikon W1 spinning disk confocal microscope using a Plan Apo TIRF 100 × 1.49 NA DIC oil-immersion objective (mitochondria-lysosome contacts, FRET) or a Nikon A1R laser scanning confocal microscope with GaAsP detectors using a Plan Apo λ 100 × 1.45 NA oil immersion objective (FRAP) using NIS-Elements. Day 70 iPSC-derived dopaminergic neurons (~1.25×10^5) or HeLa cells were seeded onto four-chamber glass bottom dishes (Cellvis; D35C4-20-1.5-N) and were imaged in a humidified, temperature-controlled chamber (37°C) at 5% CO_2. HeLa cells were transfected for 24 hours with plasmids of interest using X-tremeGENE HP (Roche; 6366546001). iPSC-derived dopaminergic neurons were transduced with lentivirus at an MOI of 5 for 7 days. Blue, green, red, and far-red images were acquired sequentially in single camera mode at 500-ms exposure time. Live cells were imaged at 1 frame every 2 to 5 s.

For FRET, HeLa cells were transfected for 24 hours with LAMP1-pmTurquoise2 (donor) and mCitrine-TOMM20 (acceptor) and imaged at excitation wavelengths of 445 and 515 nm. Excitation and emission were configured for the following: cyan fluorescent protein (CFP) excitation/CFP emission, yellow fluorescent protein (YFP) excitation/YFP emission, and CFP excitation/YFP emission. For FRAP, four to five regions of interest (ROIs) for photostimulation were randomly selected per frame. Cells were then imaged at baseline at 1 frame every 4 s for 12 s, photobleached with the 488-nm laser at 100% intensity for 15 s, and imaged again for fluorescence recovery at 1 frame every 4 s for 2 additional minutes. For localization of lentiviral Mito-IP and Lyso-IP constructs in iPSC-derived dopaminergic neurons, cells were incubated for 30 min with 50 nM MitoTracker Red (Invitrogen; M7512) or 50 nM LysoTracker DeepRed (Invitrogen; L12492), washed three times with fresh media, and subsequently imaged. For HaloTag labeling, cells were incubated with 30 nM (1:6667 of a 200 μM) stock Janelia Fluor 646 HaloTag ligand (Promega; GA1120) for 30 min, washed three times with fresh media, and subsequently imaged.

Super-resolution SIM

SIM super-resolution images were taken on a Nikon N-SIM microscope with a 100 × 1.49 NA oil-immersion objective. Images were captured and reconstructed using slice reconstruction in NIS-Elements. Images for live-cell imaging (live N-SIM) were taken at a single *z*-plane. Cells used for live-cell imaging were maintained in a temperature-controlled chamber (37°C) at 5% CO_2 in a TokaiHit stage-top incubator.

Image processing and analysis

Confocal images were processed using NIS-Elements v5.2. Time-lapse images were corrected for photobleaching using intensity equalization over time. For all experiments other than FRET and FRAP, images were processed using Denoise AI and the two-dimensional Deconvolution module in NIS-Elements.

For analysis of mitochondria-lysosome contact site dynamics, mitochondria-lysosome contacts were defined as has been previously described (*12*). The percentage of lysosomes in contact with mitochondrial was quantified as the percentage of LAMP1-Halo– or LAMP1-mGFP–positive vesicles that formed contacts with mApple-TOMM20-N-10–labeled mitochondria for greater than 10 s divided by the total number of LAMP1-Halo– or LAMP1-mGFP–positive vesicles in the ROI. The minimum duration of contacts was quantified as the time before contact untethering (mitochondria and lysosome detaching from one another) over a 3-min (180-s) video. All contacts analyzed for the minimum duration of contacts were those that had already formed at the beginning of the video, and any contacts that lasted throughout the entirety of the video were categorized as 180 s in the analysis. For analysis of mitochondria-lysosome contacts using SIM, LAMP1-mGFP and mApple-TOMM20-N-10 signals were thresholded for each cell to generate lysosomal and mitochondrial binaries. Subsequently, an overlap binary of the 488 (green) and 568 (red) channels was generated. The percentage of lysosomal area overlapping with mitochondria was calculated as the area of the overlap binary divided by the total lysosomal area.

For colocalization analysis using Pearson′s correlation coefficient, colocalization of Rab7 WT or K38R with lysosomal marker BFP-lysosomes was performed using the Colocalization module in NIS-Elements. ROIs were drawn around individual cells after

which the Pearson's correlation coefficient was calculated between the 405-nm (blue) and 488-nm (green) channels. For colocalization analysis using Pearson's correlation coefficient in cells expressing Parkin WT or C431S, all cells included in the analysis were first verified to express Halo-Parkin WT or C431S (incubated with Janelia Fluor 646 HaloTag ligand) via the 647-nm (far red) channel before application of the Colocalization module to calculate the Pearson's correlation coefficient between the 405-nm (blue) and 488-nm (green) channels.

For FRET analysis, the NIS-Elements FRET module was used to calculate sensitized emission FRET (SE-FRET) after unbiasedly generating ROIs by tracing individual cells. As described above, all cells were first verified to express Halo-Parkin WT or C431S via the 647-nm (far red) channel before analysis using the FRET module. Calculation of FRET coefficients for SE-FRET were completed using the FRET Calibration module in NIS-Elements. Briefly, a donor sample–only image (LAMP1-pmTurquoise2 with images taken at CFP excitation/CFP emission, YFP excitation/YFP emission, and CFP excitation/YFP emission) and an acceptor sample–only image (mCitrine-TOMM20 with images taken at CFP excitation/CFP emission, YFP excitation/YFP emission, and CFP excitation/YFP emission) were selected, and background intensity was subtracted using a manually drawn background ROI. After FRET coefficients were determined, FRET View in NIS-Elements was applied, and the FRET efficiency for individual cells was obtained from the ROI Statistics.

For FRAP analysis of Rab7 on lysosomes, NIS-Elements was used to threshold and create an overlap binary between LAMP1-RFP and eGFP-Rab7 WT. The total intensity of the 488-nm (green) channel in the overlap binary, corresponding to the eGFP-Rab7 WT signal colocalized with LAMP1-RFP, was averaged over the 15 s of baseline (prephotobleaching) time-lapse microscopy. The intensity of green fluorescence in the overlap binary after photobleaching (t = 0 s) was measured every 4 s as a percentage of baseline intensity of green fluorescence in the overlap binary to generate a FRAP tracing. The FRAP recovery rate was calculated as average of the slopes of the best-fit line for the FRAP tracings of each cell included in the analysis. In addition, the fraction of fluorescence recovery of eGFP-Rab7 WT was also calculated at 30, 60, and 90 s after photobleaching. As previously mentioned, cells included in the analysis were first verified to express Halo-Parkin WT or C431S via the 647-nm (far red) channel.

Statistical analysis, graphing, and figure assembly

Data were analyzed using unpaired or paired two-tailed Student's t test (for two datasets) or one-way analysis of variance (ANOVA) with Tukey's or Dunnett's post hoc test (for multiple datasets). Data presented are means ± SEM. All statistical tests were justified as appropriate and were analyzed from $n \geq 9$ cells (for live-cell imaging experiments, see text and figure legends for details). All experiments were also conducted from $n \geq 3$ independent experiments (biological replicates) per condition. Statistics and graphing were performed using Prism 9.0 (GraphPad) and R software. Videos and images were processed and assembled using NIS-Elements. All figures were assembled using Microsoft Powerpoint and Adobe Illustrator.

Supplementary Materials

This PDF file includes:
Figs. S1 to S6
Legends for tables S1 to S3

Other Supplementary Material for this manuscript includes the following:
Tables S1 to S3

View/request a protocol for this paper from *Bio-protocol*.

REFERENCES AND NOTES

1. W. Poewe, K. Seppi, C. M. Tanner, G. M. Halliday, P. Brundin, J. Volkmann, A. E. Schrag, A. E. Lang, Parkinson disease. *Nat. Rev. Dis. Primers* **3**, 17013 (2017).
2. L. F. Burbulla, P. Song, J. R. Mazzulli, E. Zampese, Y. C. Wong, S. Jeon, D. P. Santos, J. Blanz, C. D. Obermaier, C. Strojny, J. N. Savas, E. Kiskinis, X. Zhuang, R. Krüger, D. J. Surmeier, D. Krainc, Dopamine oxidation mediates mitochondrial and lysosomal dysfunction in Parkinson's disease. *Science* **357**, 1255–1261 (2017).
3. W. Peng, G. Minakaki, M. Nguyen, D. Krainc, Preserving lysosomal function in the aging brain: Insights from neurodegeneration. *Neurotherapeutics* **16**, 611–634 (2019).
4. M. Nguyen, Y. C. Wong, D. Ysselstein, A. Severino, D. Krainc, Synaptic, mitochondrial, and lysosomal dysfunction in Parkinson's disease. *Trends Neurosci.* **42**, 140–149 (2019).
5. C. Klein, A. Westenberger, Genetics of Parkinson's disease. *Cold Spring Harb. Perspect. Med.* **2**, a008888 (2012).
6. K. S. Marder, M. X. Tang, H. Mejia-Santana, L. Rosado, E. D. Louis, C. L. Comella, A. Colcher, A. D. Siderowf, D. Jennings, M. A. Nance, S. Bressman, W. K. Scott, C. M. Tanner, S. F. Mickel, H. F. Andrews, C. Waters, S. Fahn, B. M. Ross, L. J. Cote, S. Frucht, B. Ford, R. N. Alcalay, M. Rezak, K. Novak, J. H. Friedman, R. F. Pfeiffer, L. Marsh, B. Hiner, G. D. Neils, M. Verbitsky, S. Kisselev, E. Caccappolo, R. Ottman, L. N. Clark, Predictors of parkin mutations in early-onset Parkinson disease: The consortium on risk for early-onset Parkinson disease study. *Arch. Neurol.* **67**, 731–738 (2010).
7. D. Narendra, A. Tanaka, D. F. Suen, R. J. Youle, Parkin is recruited selectively to impaired mitochondria and promotes their autophagy. *J. Cell Biol.* **183**, 795–803 (2008).
8. J. H. Shin, H. S. Ko, H. Kang, Y. Lee, Y. I. Lee, O. Pletinkova, J. C. Troconso, V. L. Dawson, T. M. Dawson, PARIS (ZNF746) repression of PGC-1α contributes to neurodegeneration in Parkinson's disease. *Cell* **144**, 689–702 (2011).
9. P. Song, K. Trajkovic, T. Tsunemi, D. Krainc, Parkin modulates endosomal organization and function of the endo-lysosomal pathway. *J. Neurosci.* **36**, 2425–2437 (2016).
10. C. Vives-Bauza, C. Zhou, Y. Huang, M. Cui, R. L. de Vries, J. Kim, J. May, M. A. Tocilescu, W. Liu, H. S. Ko, J. Magrané, D. J. Moore, V. L. Dawson, R. Grailhe, T. M. Dawson, C. Li, K. Tieu, S. Przedborski, PINK1-dependent recruitment of Parkin to mitochondria in mitophagy. *Proc. Natl. Acad. Sci. U.S.A.* **107**, 378–383 (2010).
11. Y. Lee, D. A. Stevens, S. U. Kang, H. Jiang, Y. I. Lee, H. S. Ko, L. A. Scarffe, G. E. Umanah, H. Kang, S. Ham, T. I. Kam, K. Allen, S. Brahmachari, J. W. Kim, S. Neifert, S. P. Yun, F. C. Fiesel, W. Springer, V. L. Dawson, J. H. Shin, T. M. Dawson, PINK1 primes Parkin-mediated ubiquitination of PARIS in dopaminergic neuronal survival. *Cell Rep.* **18**, 918–932 (2017).
12. Y. C. Wong, D. Ysselstein, D. Krainc, Mitochondria-lysosome contacts regulate mitochondrial fission via RAB7 GTP hydrolysis. *Nature* **554**, 382–386 (2018).
13. Y. C. Wong, S. Kim, W. Peng, D. Krainc, Regulation and function of mitochondria-lysosome membrane contact sites in cellular homeostasis. *Trends Cell Biol.* **29**, 500–513 (2019).
14. Y. C. Wong, W. Peng, D. Krainc, Lysosomal regulation of inter-mitochondrial contact fate and motility in Charcot-Marie-tooth type 2. *Dev. Cell* **50**, 339–354.e4 (2019).
15. W. Peng, Y. C. Wong, D. Krainc, Mitochondria-lysosome contacts regulate mitochondrial Ca(2+) dynamics via lysosomal TRPML1. *Proc. Natl. Acad. Sci. U.S.A.* **117**, 19266–19275 (2020).
16. Y. C. Wong, S. Kim, J. Cisneros, C. G. Molakal, P. Song, S. J. Lubbe, D. Krainc, Mid51/Fis1 mitochondrial oligomerization complex drives lysosomal untethering and network dynamics. *J. Cell Biol.* **221**, e202206140 (2022).
17. C. Y. Lim, O. B. Davis, H. R. Shin, J. Zhang, C. A. Berdan, X. Jiang, J. L. Counihan, D. S. Ory, D. K. Nomura, R. Zoncu, ER-lysosome contacts enable cholesterol sensing by mTORC1 and drive aberrant growth signalling in Niemann-Pick type C. *Nat. Cell Biol.* **21**, 1206–1218 (2019).
18. S. Kim, Y. C. Wong, F. Gao, D. Krainc, Dysregulation of mitochondria-lysosome contacts by GBA1 dysfunction in dopaminergic neuronal models of Parkinson's disease. *Nat. Commun.* **12**, 1807 (2021).

19. L. Cantarero, E. Juárez-Escoto, A. Civera-Tregón, M. Rodríguez-Sanz, M. Roldán, R. Benítez, J. Hoenicka, F. Palau, Mitochondria-lysosome membrane contacts are defective in GDAP1-related Charcot-Marie-Tooth disease. *Hum. Mol. Genet.* **29**, 3589–3605 (2021).
20. J. B. Spinelli, M. C. Haigis, The multifaceted contributions of mitochondria to cellular metabolism. *Nat. Cell. Biol.* **20**, 745–754 (2018).
21. A. Efeyan, R. Zoncu, D. M. Sabatini, Amino acids and mTORC1: From lysosomes to disease. *Trends Mol. Med.* **18**, 524–533 (2012).
22. C. E. Hughes, T. K. Coody, M. Y. Jeong, J. A. Berg, D. R. Winge, A. L. Hughes, Cysteine toxicity drives age-related mitochondrial decline by altering iron homeostasis. *Cell* **180**, 296–310.e18 (2020).
23. M. Abu-Remaileh, G. A. Wyant, C. Kim, N. N. Laqtom, M. Abbasi, S. H. Chan, E. Freinkman, D. M. Sabatini, Lysosomal metabolomics reveals V-ATPase- and mTOR-dependent regulation of amino acid efflux from lysosomes. *Science* **358**, 807–813 (2017).
24. W. W. Chen, E. Freinkman, T. Wang, K. Birsoy, D. M. Sabatini, Absolute quantification of matrix metabolites reveals the dynamics of mitochondrial metabolism. *Cell* **166**, 1324–1337.e11 (2016).
25. D. Höglinger, T. Burgoyne, E. Sanchez-Heras, P. Hartwig, A. Colaco, J. Newton, C. E. Futter, S. Spiegel, F. M. Platt, E. R. Eden, NPC1 regulates ER contacts with endocytic organelles to mediate cholesterol egress. *Nat. Commun.* **10**, 4276 (2019).
26. J. Cisneros, T. B. Belton, G. C. Shum, C. G. Molakal, Y. C. Wong, Mitochondria-lysosome contact site dynamics and misregulation in neurodegenerative diseases. *Trends Neurosci.* **45**, 312–322 (2022).
27. O. Griesbeck, G. S. Baird, R. E. Campbell, D. A. Zacharias, R. Y. Tsien, Reducing the environmental sensitivity of yellow fluorescent protein. Mechanism and applications. *J. Biol. Chem.* **276**, 29188–29194 (2001).
28. J. M. Falcón-Pérez, R. Nazarian, C. Sabatti, E. C. Dell'Angelica, Distribution and dynamics of Lamp1-containing endocytic organelles in fibroblasts deficient in BLOC-3. *J. Cell Sci.* **118**, 5243–5255 (2005).
29. J. Goedhart, D. von Stetten, M. Noirclerc-Savoye, M. Lelimousin, L. Joosen, M. A. Hink, L. van Weeren, T. W. Gadella Jr., A. Royant, Structure-guided evolution of cyan fluorescent proteins towards a quantum yield of 93%. *Nat. Commun.* **3**, 751 (2012).
30. X. Jiang, C. Zhang, J. Chen, S. Choi, Y. Zhou, M. Zhao, X. Song, X. Chen, M. Maletić-Savatić, T. Palzkill, D. Moore, M. C. Wang, J. Wang, Quantitative real-time imaging of glutathione with subcellular resolution. *Antioxid. Redox Signal* **30**, 1900–1910 (2019).
31. J. F. Trempe, V. Sauvé, K. Grenier, M. Seirafi, M. Y. Tang, M. Ménade, S. Al-Abdul-Wahid, J. Krett, K. Wong, G. Kozlov, B. Nagar, E. A. Fon, K. Gehring, Structure of parkin reveals mechanisms for ubiquitin ligase activation. *Science* **340**, 1451–1455 (2013).
32. Q. Sun, W. Westphal, K. N. Wong, I. Tan, Q. Zhong, Rubicon controls endosome maturation as a Rab7 effector. *Proc. Natl. Acad. Sci. U.S.A.* **107**, 19338–19343 (2010).
33. N. M. Sherer, M. J. Lehmann, L. F. Jimenez-Soto, A. Ingmundson, S. M. Horner, G. Cicchetti, P. G. Allen, M. Pypaert, J. M. Cunningham, W. Mothes, Visualization of retroviral replication in living cells reveals budding into multivesicular bodies. *Traffic* **4**, 785–801 (2003).
34. K. Romero Rosales, E. R. Peralta, G. G. Guenther, S. Y. Wong, A. L. Edinger, Rab7 activation by growth factor withdrawal contributes to the induction of apoptosis. *Mol. Biol. Cell* **20**, 2831–2840 (2009).
35. S. Kriks, J. W. Shim, J. Piao, Y. M. Ganat, D. R. Wakeman, Z. Xie, L. Carrillo-Reid, G. Auyeung, C. Antonacci, A. Buch, L. Yang, M. F. Beal, D. J. Surmeier, J. H. Kordower, V. Tabar, L. Studer, Dopamine neurons derived from human ES cells efficiently engraft in animal models of Parkinson's disease. *Nature* **480**, 547–551 (2011).
36. L. F. Burbulla, S. Jeon, J. Zheng, P. Song, R. B. Silverman, D. Krainc, A modulator of wild-type glucocerebrosidase improves pathogenic phenotypes in dopaminergic neuronal models of Parkinson's disease. *Sci. Transl. Med.* **11**, eaau6870 (2019).
37. C. Trapnell, A. Roberts, L. Goff, G. Pertea, D. Kim, D. R. Kelley, H. Pimentel, S. L. Salzberg, J. L. Rinn, L. Pachter, Differential gene and transcript expression analysis of RNA-seq experiments with TopHat and Cufflinks. *Nat. Protoc.* **7**, 562–578 (2012).
38. S. Anders, P. T. Pyl, W. Huber, HTSeq—a Python framework to work with high-throughput sequencing data. *Bioinformatics* **31**, 166–169 (2015).
39. M. D. Robinson, D. J. McCarthy, G. K. Smyth, edgeR: A bioconductor package for differential expression analysis of digital gene expression data. *Bioinformatics* **26**, 139–140 (2010).
40. Y. Liao, J. Wang, E. J. Jaehnig, Z. Shi, B. Zhang, WebGestalt 2019: Gene set analysis toolkit with revamped UIs and APIs. *Nucleic Acids Res.* **47**, W199–w205 (2019).
41. M. Kanehisa, Y. Sato, KEGG Mapper for inferring cellular functions from protein sequences. *Protein Sci.* **29**, 28–35 (2020).
42. Z. Pang, J. Chong, G. Zhou, D. A. de Lima Morais, L. Chang, M. Barrette, C. Gauthier, P. Jacques, S. Li, J. Xia, MetaboAnalyst 5.0: Narrowing the gap between raw spectra and functional insights. *Nucleic Acids Res.* **49**, W388–W396 (2021).

Acknowledgments: We thank all members of the Krainc laboratory for helpful advice. All imaging was performed at the Northwestern University Center for Advanced Microscopy supported by CCSF P30 CA060553 awarded to the Robert H. Lurie Comprehensive Cancer Center. Transcriptomics services were performed by the Northwestern University NUSeq Core Facility. Metabolomics services were performed by the Northwestern University Metabolomics Core Facility at the Robert H. Lurie Comprehensive Cancer Center. **Funding:** This work was supported by the following grants: National Institutes of Health AG066333 (W.P.), National Institutes of Health NS109252 (Y.C.W.), and National Institutes of Health NS122257 (D.K.). **Author contributions:** Conceptualization: W.P., Y.C.W., and D.K. Methodology: W.P., Y.C.W., and D.K. Formal analysis: W.P. Investigation: W.P. and L.F.S. Resources: W.P. and P.S. Writing—original draft: W.P., L.F.S., and Y.C.W. Writing—review and editing: W.P., Y.C.W., and D.K. Supervision: Y.C.W. and D.K. Funding acquisition: W.P., Y.C.W., and D.K. **Competing interests:** D.K. is the Founder and Scientific Advisory Board Chair of Vanqua Bio; serves on the scientific advisory boards of The Silverstein Foundation, Intellia Therapeutics, and AcureX Therapeutics; and is a Venture Partner at OrbiMed. The authors declare that they have no other competing interests. **Data and materials availability:** All data needed to evaluate the conclusions in the paper are present in the paper and/or the Supplementary Materials. Original data for the paper have also been deposited on Dryad (https://doi.org/10.5061/dryad.sqv9s4n81).

Submitted 27 February 2023
Accepted 15 June 2023
Published 19 July 2023
10.1126/sciadv.adh3347